Transient Simulation of Cavitation in a Turbopump Inducer

By Christopher GROLL,[1,2)] Tobias TRAUDT,[2)] and Jan DEEKEN,[2)] and Stefan SCHLECHTRIEM[2)]

[1)] *Institute of Space Systems, The University of Stuttgart, Stuttgart, Germany*
[2)] *Institute of Space Propulsion, DLR, Hardthausen, Germany*

This paper investigates the transient behavior of the cavitation process inside a three-bladed flat-plate inducer and how it can be influenced by the introduction of flow co-rotation in the inducer inlet by means of tangential fluid injection. The models necessary for the reproduction of the transient behavior of a cavity forming at the leading edge are implemented in the OpenFOAM software package and validated against experimental data from literature. The generated numerical setup is then applied to the inducer geometry. The transient 3D simulation of the complete inducer indicates that the introduction of inlet flow co-rotation in the vicinity of the blade tips by means of tangential fluid injection leads to a reduction in vapor content in the simulation domain alongside an alteration of the pressure fluctuations detected in the inducer outlet and thereby the transient forces acting on the inducer blades.

Key Words: Cavitation, Inducer, Turbopump

Nomenclature

c	:	velocity, m/s
d	:	diameter, m
f	:	frequency, Hz
g	:	gravitational acceleration, m/s^2
h	:	blade height, m
l	:	length, m
$\dot{m}$	:	phase change rate, kg/sm^3
p	:	pressure, Pa
R	:	radius, m
S	:	source, -
x	:	position, -
y_+	:	dimensionless wall distance , -
α	:	void fraction, -
μ	:	dynamic viscosity, Pa s
ν	:	kinematic viscosity, m^2/s
ρ	:	density, kg/m^3
ω	:	specific rate of dissipation, 1/s
Subscripts		
ave	:	average
B	:	bubble
cond	:	condensation
evap	:	evaporation
h	:	hydraulic
in	:	inlet
l	:	liquid
lim	:	limit
m	:	mixture
nuc	:	nucleation site
ps	:	pressure side
r	:	relative
sat	:	saturation
ss	:	suction side
t	:	turbulence
u	:	circumferential
v	:	vapor
x	:	x-component

1. Introduction

In order to achieve combustion chamber pressures necessary for main stage propulsion systems to reach relevant performances, while also maintaining an acceptable system dry mass, propellant pumps are a necessity. Considering that the mass of the feed system is dominated by the mass of the tanks it is also clear, that low tank pressures and thereby low pump inlet pressures are desirable. However, a compact and therefore light pump needs to operate at high rotational rates. High relative speeds between pumped fluid and pump impeller blades in tandem with low pump inlet pressures make cavitation a concern. This phenomenon can both influence pump performance as well as lifetime. Here the influence on lifetime stems from the transient force exerted by the growth, collapse or shedding of cavities. In order to mitigate the influence of cavitation on pump performance, propellant pumps found in space propulsion, but also aviation applications, are commonly outfitted with inducers.[1)] These axial pumps are placed on the pump shaft just upstream of the impeller. They can provide a pressure increase of up to 10% of the pressure rise generated by the pump.[2)] The spacing and design of the blades enables them to operate under partial cavitation without losing their ability to provide adequate inlet pressures to the main stage(s) of the pump. Inducer blades usually consist of a sharp leading edge which slowly transitions to a thin main blade. This makes material fatigue a concern. In order to limit transient blade loads, groves may be placed in the inducer housing in order to reduce the influence of tip leakage via its interaction with adjacent blades. The shape of the blade leading edges may also be modified into an arc as another approach to limit blade interaction.[3,4)] For stationary applications in industry a row of adjustable stators, similar to what may be encountered in axial compressors, may be included in order to influence the inducer inlet velocity and thereby incidence angle in order to react to varying operating conditions and limit flow separation or cavitation causing undesirable machine behavior or blade loads.[5)] This approach is not seen as desirable in space propulsion applications due to the need for additional actuators and motion feedthroughs which

need to stand up to adverse mechanical, thermal and chemical environments while maintaining a gas tight seal. As with the inducer or impeller blades themselves, the casing treatment geometry is also fixed, and thereby limited in operating range or efficiency. In a previous publication the introduction of flow co-rotation at the inlet of the pump, by means of tangential injection of fluid upstream of the inducer, was investigated as an approach to cavitation control and therefore transient mechanical load mitigation approach.[6] The fluid utilized for injection is sourced either form the leakage though the front floating ring seal or extracted from the pump outlet though a dedicated return pipe. In order to evaluate the effect of this injection, a series of steady state simulations were performed both with and without inlet flow rotation. It was found that the cavitation curves did not differ significantly and that cavitation stall was reached at similar inlet pressures for both configurations. It was theorized that the impact of reduced relative velocity at the inducer blade tips might postpone the development of cloud cavitation. This would be desirable, as transient loads on the blade and the bearings supporting the turbopump shaft would be reduced, potentially increasing the turbopump's lifetime. This paper presents transient cavitation simulations in the 3D inducer geometry previously employed in steady state simulations. In a first step cloud cavitation in a converging/diverging nozzle is simulated. Here the experimental and numerical work of Stutz and Coutier-Delghosa act as a reference since they are widely used in literature for model validation.[7–10] The nozzle at the focus of their work also represents a simplified inducer blade geometry, making it applicable to the case discussed in this paper. It is reported that the standard two equation turbulence models, such as the widely used k-w SST turbulence model fail to reproduce the periodic shedding of the cavity formed at the nozzle throat. This is found to be the case due to an overprediction of the eddy viscosity at the interface between vapor and liquid phase which in turn suppresses the formation of a re-entrant jet that would otherwise drive the shedding process.[11–13] The proposed solution is the introduction of a correction which limits the eddy viscosity as a function of void fraction. For the simulations conducted in the scope of this paper this modification is implemented for the k-w SST turbulence model in OpenFOAM v2306.[14] Furthermore, numerical parameters such as discretization and solution strategy applied in the approximation of the governing equations are adjusted such that the experimentally determined shedding frequency on one hand, and numerical stability for the application to complex geometries on the other hand, are combined. This setup is then applied to the full three-dimensional inducer geometry to conduct a series of transient simulations. The full 3D simulations are evaluated using both function objects which sample pressure and vapor content in the simulation domain at the end of every iteration as well as via the export of 720 states of the entire flow field, representing two full inducer rotations.

This paper therefore not only aims at continuing the investigation started in the preceding publication but also presents information concerning the implementation of the turbulence model changes proposed in literature, the selection of boundary and initial conditions for both the validation case as well as for the full machine while also giving an insight into the numerical setup and capabilities of OpenFOAM concerning turbopump investigations.

2. Model Selection, Implementation and Validation

In preceding works, cavitation within the pumps developed at DLR's Institute of Space Propulsion was evaluated via a series of steady state simulations conducted for decreasing pump inlet pressures. With this an estimate of the inlet pressure at which cavitation stall would occur could be obtained, aiding in the definition of safe test conditions for the LUMEN turbopumps.[15] Since the Volume-of-Fluid (VoF) and transport equation based simulation of cavitation used in previous investigations yielded satisfactory results, it is decided to also apply this approach to modeling transient phase change in rotating machinery.

OpenFOAM includes a wide variety of solvers out of the box. The presented simulations employ the interPhaseChangeDyMFoam solver which handles two isothermal and immiscible fluids while enabling phase change via a series of already implemented phase change models. OpenFOAM solves the governing equations, as given in Eqs. 1, 2 and 3 for the phase mixture, as described in Eqs. 6 and 7, according to user inputs. In the presented simulations surface tension is neglected as it is found that it's contribution to the vapor distribution in the reference experiment used for model calibration is not substantial.

$$\nabla \cdot \mathbf{u} = 0 \tag{1}$$

$$\frac{\partial \rho \mathbf{u}}{\partial t} + \nabla \cdot \rho \mathbf{u}\mathbf{u}^T - \nabla \cdot \left[\mu \left(\nabla \mathbf{u} + \nabla \mathbf{u}^T\right)\right] = -\nabla p_{rgh} - (\mathbf{g} \cdot \mathbf{x}) \nabla \rho \tag{2}$$

$$\frac{\partial \alpha}{\partial t} + \nabla \alpha \mathbf{u} + \nabla \left[\alpha \left(1 - \alpha\right) \mathbf{u}_r\right] + S = 0 \tag{3}$$

Here the static pressure is denoted with $p_{rgh} = p - \mathbf{g}\mathbf{x}$. As in the preceding works, the Schnerr-Sauer model is selected to facilitate mass transfer between the phases. It describes condensation and evaporation as a process purely driven by the difference between static and vapor pressure while considering the presence of nucleation sites as well as the presence of preexisting vapor, as described in Eq. 4 and 5.[16]

$$\dot{m}_{evap} = \frac{\rho_v \rho_l}{\rho_m} \alpha (1 - \alpha) \frac{3}{R_B} \sqrt{\frac{2}{3} \frac{(p_{sat} - p)}{\rho_l}} \tag{4}$$

$$\dot{m}_{cond} = \frac{\rho_v \rho_l}{\rho_m} \alpha (1 - \alpha) \frac{3}{R_B} \sqrt{\frac{2}{3} \frac{(p - p_{sat})}{\rho_l}} \tag{5}$$

$$\rho_m = (1 - \alpha)\rho_l + \alpha \rho_v \tag{6}$$

$$\nu_m = (1 - \alpha)\nu_l + \alpha \nu_v \tag{7}$$

Details concerning the discretization applied in the presented simulations are given in section **2.3.**.

The standard parameters of the model for water are applied, as shown in Table 1, which also lists the fluid properties applied in the presented simulations. These properties are derived from the work by Decaix and Goncalves who investigated the same problem.[11]

Table 1.: Cavitation model parameters and fluid properties.

Parameter	Value
n	1.6E13
d_{nuc}	2E-6 m
p_{sat}	2339.3 Pa
ν_l	1.00341E-6 m^2/s
ρ_l	998.19 kg/m^3
ν_v	3.7796E-4 m^2/s
ρ_v	1.7314E-2 kg/m^3

In order to enable the shedding of cavities while applying standard two-equation turbulence modes, an eddy viscosity limiter $\nu_{t,lim}$ needs to be implemented, as reported by Reboud.[12] Without this modification an overestimation of viscosity in the vicinity of the phase boundary prohibits the reproduction of realistic flow physics. Specific to the case discussed here, this leads to the suppression of the so-called re-entrant jet, a liquid patch flowing from the cavity closure region to the leading edge of the cavitating surface, where it is one of the factors which can lead to the shedding of a cavity.[11,12]

Here this adaptation is implemented as shown in equation 8.

$$\nu_{t,lim} = \rho_v + \left(\frac{\rho_v - \rho_m}{\rho_v - \rho_l}\right)^n \tag{8}$$

This expression is included in the eddy viscosity computation step of the turbulence model, in this case k-w SST, as indicated in equation 9.

$$\nu_t = \nu_{t,lim} a_1 \frac{k}{max(a_1\omega, b_1 F_{23} S)} \tag{9}$$

Here a_1, b_1, F_{23} and S are model parameters while k and ω represent turbulence kinetic energy and specific dissipation rate, respectively.[14]

After conducting a series of numerical experiments, the exponent n is set to 4 as this most closely reproduced the experimentally observed shedding frequency for the reference case that is employed for model calibration.

2.1. Reference Case Description

The experiment conducted by Reboud serves as the basis for a wide variety of numerical studies.[8,11] Here a cavitating converging diverging nozzle is examined using invasive optical probes as well as wall mounted pressure transducers. Additionally, high speed video is taken of the region of interest downstream of the nozzle throat. A relationship between system pressure, flow velocity and shedding frequency is reported. This case is selected for the study presented here as the diverging section of the nozzle is designed to represent a simplified form of the suction side of a typical inducer blade while being computationally inexpensive enough for parameter studies necessary to reproduce experimental data.[8] Figure 1 gives an overview of the nozzle geometry as well as the dimensions of the simulation domain derived from the reported experimental work.

2.2. Mesh

A quasi 2D simulation domain is defined according to the geometry shown in Fig. 1. Using the OpenFOAM blockmesh utility, two structured meshes are generated. In reference to results

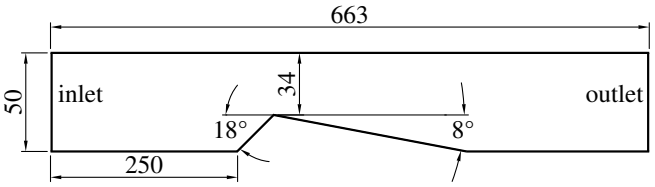

Fig. 1.: Sketch of the simulation domain indicating major dimensions as well as the locations of inlet and outlet.


Fig. 2.: Overview of the coarse mesh.

reported by Reboud et al., a high y+ mesh is generated consisting of 60x215 cells.[13] Furthermore, a low y+ mesh consisting of 150 x 400 cells is generated in order to evaluate the influence of mesh resolution in the bulk flow as well as the usage of wall functions on the development of cloud cavitation. Both meshes consist of four blocks covering the inlet, convergent, divergent and outlet sections. These blocks exhibit constant growth rates towards the center line of the channel. While the coarse mesh features an initial cell height of $1.43E-4m$ and an expansion rate from the top and bottom walls of 1.1 this is reduced to $5.36E-6m$ and 1.05 respectively for the fine mesh. Furthermore, axial cell expansion rates around the throat of the nozzle are set for both cases such that low aspect ratio cells can be found in the mesh region where the cavity closure is expected to occur. An overview of the coarse mesh is given in Fig. 2. Closeups for both meshes are shown in Fig. 3 alongside an indication of cell size. Figure 4 shows plots of the dimensionless wall distance derived from data obtained over three seconds of simulation time for each of the meshes. Note that the location of the nozzle throat defines the origin of the coordinate system used to present the generated results.

2.3. Numerical Setup

This section describes the configuration employed in both the reference case as well as full inducer simulations. In a first step a combination of numerical schemes and solution algorithms is defined and applied to the reference case. When a setup generates the reported cloud cavity shedding frequency while also exhibiting stable behavior it is applied to the inducer case. With the goal of high accuracy as well as stability, a wide variety of numerical schemes have been investigated. Due to the low non-orthogonality and skewness of the cells found in the structured mesh of the reference case, it lends itself to the application of second order accurate schemes which would otherwise be susceptible to spurious oscillation. Such a setup cannot be applied to more imperfect mesh made necessary by the complex shape of the inducer investigated in this study. The application of OpenFOAM's "limitedLinear" scheme to the advection terms for velocity and turbulence quantities yielded good results. This scheme allows to limiting towards upwind in regions of steep gradients while tending towards central differencing in less active regions of the flow field. Further control is awarded to the user by prescribing a weighing factor which adjusts the impact of the flux limiter. Here a coefficient of 0.2 was found to be a suitable compromise between accuracy and stability while minimizing the presence of oscillations observed when applying pure central differencing. Further iterations, extending to the use of different meshing strategies for the inducer

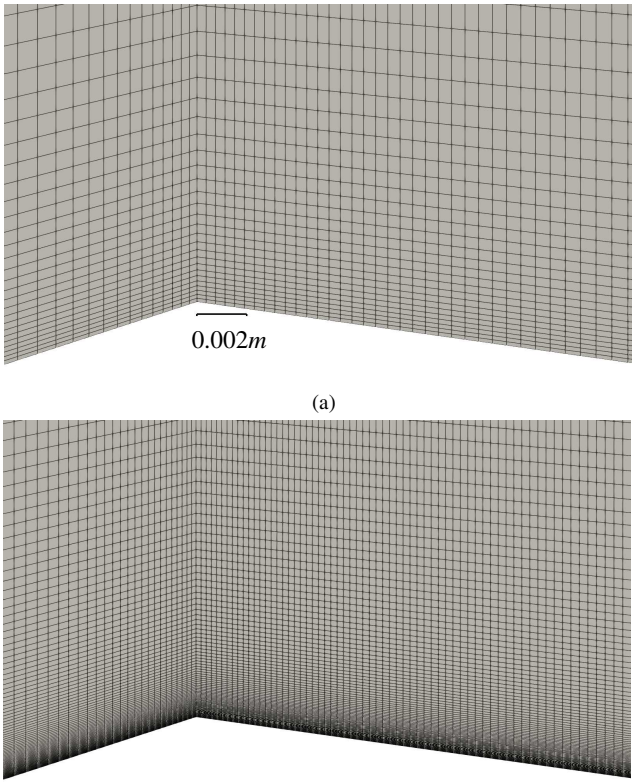

Fig. 3.: Detailed view of coarse (3a) and fine (3b) mesh in the throat region alongside an indication of cell size.

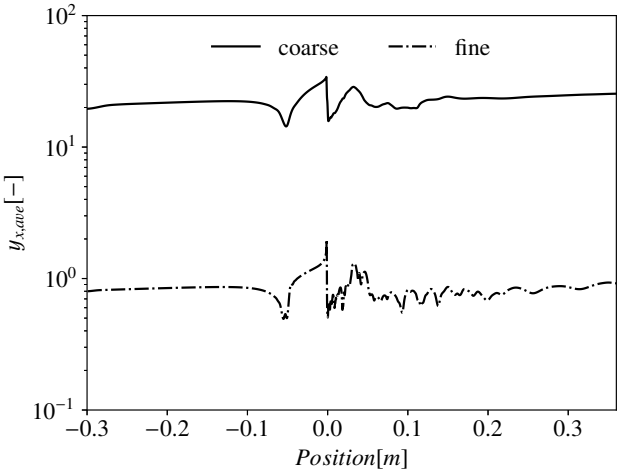

Fig. 4.: Plot of time averaged dimensionless wall distance for both investigated meshes.

employing both commercial and open source tools, yielded the final configuration which is now free of oscillations and robust enough to forgo time consuming initialization of the flow field throughout the inducer / impeller flow domain. As no significant influence of the discretization approach of the turbulence model field variables was identified, it is elected to employ an upwind scheme, ensuring boundedness and stability while accepting the introduced diffusion. The largest influence on shedding frequency is identified in the method selected for the advection of velocity, leading to the selection of the unbounded second order accurate linearUpwind scheme.[17] The calculation of gradients for all fields is facilitated via cell limited linear

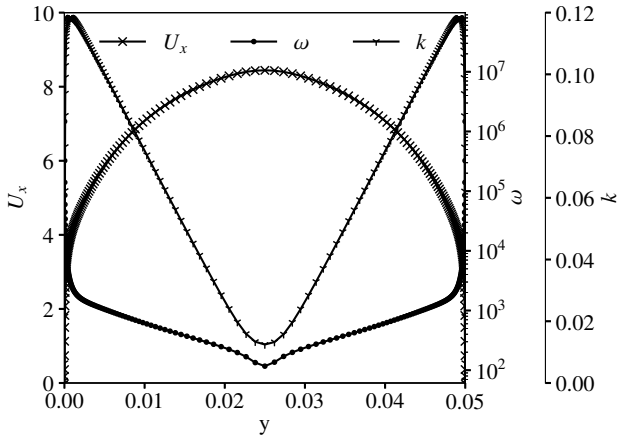

Fig. 5.: Profiles imposed over the height of the inlet of the simulation domain shown in Fig. 1.

interpolation between adjacent cell centers. Here the keyword cellLimited can be specified by the user alongside and integer between 0 and 1.

The time step is set to 5e-6 s, resulting in a mean Courant number of 0.01 while limiting the maximum present at the nozzle throat to 0.3 for the coarse mesh. For the fine mesh the time step is reduced to 1e-6 s with mean and maximum Courant numbers of 0.005 and 0.5, respectively.

Furthermore, OpenFOAM provides a wide variety of solvers for the linearized equations. Here no noteworthy variations stability or performance were observed. However, moving to more complex or larger meshes scaling should be considered in more detail.

2.4. Boundary Conditions and Initialization

No slip conditions are applied to the top and bottom walls. Wall functions are applied for calculations performed on the coarse mesh only. The inlet boundary conditions for velocity, turbulent kinetic energy and specific turbulence dissipation rate are prescribed as profiles over the channel height, as shown in Fig. 5. These values are calculated using the boundaryFoam solver while specifying an average inlet velocity of 7.04 m/s, as reported by Goncalves and Decaix.[8,11]

The simulation domain is initialized with a static pressure of 200 kPa while the liquid is assumed to be at rest. The outlet static pressure, defined on the outlet boundary, is initially also set to 200 kPa. After 0.01 s the static outlet pressure is reduced until an inlet pressure of 52 kPa is achieved, adhering to the reported experimental conditions.[8] As strong pressure oscillations are present throughout the simulation domain this process was performed iteratively.

2.5. Reference Case Results

With the coarse mesh reproduced from the information given in the publications of Reboud and iterations between flow simulation and initial cell height in order to reach a y_+ somewhat consistent with previous studies, the simulation setup and models are calibrated.[13] It is found that the standard cavitation model parameters, as stated in table 1, alongside the aforementioned empirical constant $n = 4$ in the viscosity limiter can result in a shedding frequency close to the $45Hz$ reported for the geometry and boundary conditions at hand. Besides the configuration of the models, the setup of the solution strategy indi-

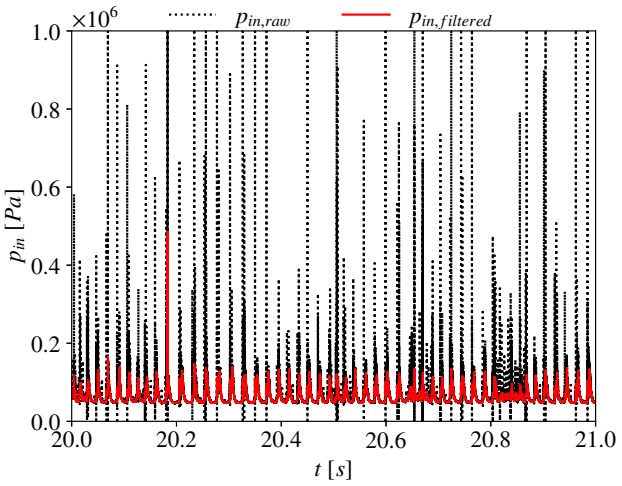

Fig. 6.: Plot of the area averaged pressure at the inlet boundary.

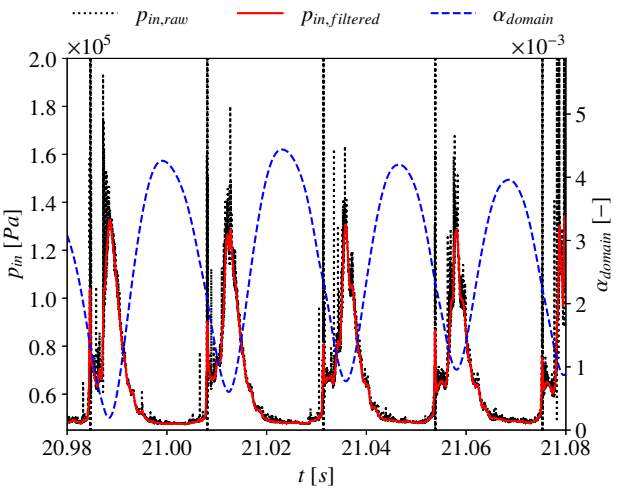

Fig. 7.: Plot of raw as well as filtered inlet pressure alongside simulation domain void fraction.

cates that the order of the time discretization scheme has no substantial influence on the generated shedding frequency. However, OpenFOAM's second order implicit "backward" scheme is applied in the presented results. As described in the preceding section, the outlet pressure is varied until an inlet pressure closely reproducing the experimental value is found. To this end, an area average of the inlet pressure is calculated each iteration. Figure 6 shows a representative portion of the gathered data.

The presence of a large number of pressure spikes can be observed which originate from the large volume changes associated with the formation, detachment and collapse of cavities in this incompressible, viscous simulation. With these spikes, the calculation of an average inlet pressure was shown to lead to an overestimation of the inlet pressure when the reproduction of experimental observations is the goal. Therefore, as a first approach a gaussian filter is applied to the sampled data in order to diminish the influence of these possibly nonphysical spikes.[18)]

Figure 7 shows the details of the progression of inlet pressure around one pressure spike. Here unaltered simulation data, filtered data as well as the void fraction present in the simulation domain are plotted.

A pattern of two pressure spikes in close proximity can be identified. A large peak in the raw data is prescient first as the domain vapor content decreases, followed by a peak of lower magnitude which coincides with a minimum in domain vapor content. The first peak can therefore be related to the initial detachment of the cavity formed at the nozzle throat while the second peak indicates the collapse and condensation of the detached vapor.

Alternative to taking the average of the filtered inlet pressure, a kernel density estimate plot is generated from the raw data in order to identify the most likely pressure present at the inlet over the evaluated time period. As can be seen in Fig. 8, the most likely inlet pressure closely reproduces the experimentally observed 52 kPa. It is also apparent that the distribution is skewed towards higher pressures due to the presence of high-pressure peaks associated with domain vapor volume changes.

Finally, the frequency content of the filtered and unfiltered inlet pressure samples is evaluated. The power spectral density (PSD) is plotted in Fig. 9 shows a clear peak in both data

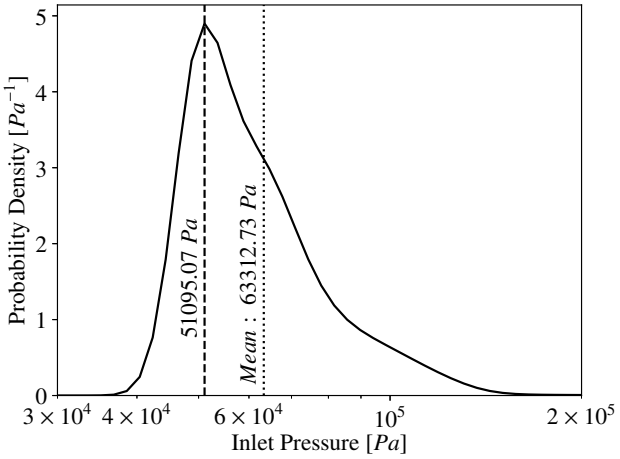

Fig. 8.: Plot of the kernel density estimate of the raw inlet pressure samples, also indicating the mean of the processed data.

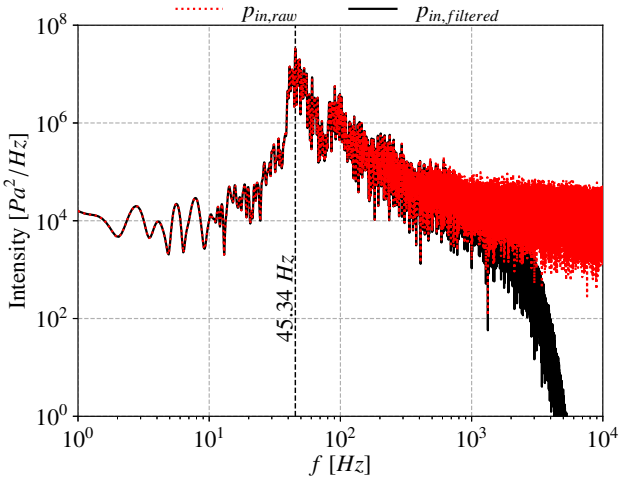

Fig. 9.: PSD-Plot of the area averaged inlet pressure indicating a maximum at a frequency of ca. 45 Hz for both filtered and unfiltered pressure data.

sets with the filtered data exhibiting less noise in the higher frequency range.

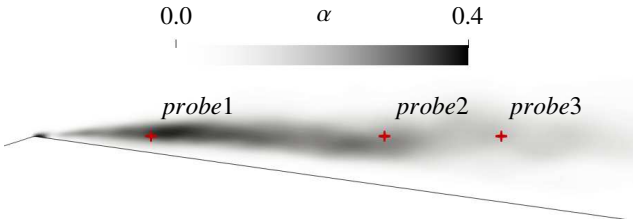

Fig. 10.: Plot of time averaged vapor content in the vicinity of the nozzle throat. Probe locations are indicated by red crosses.

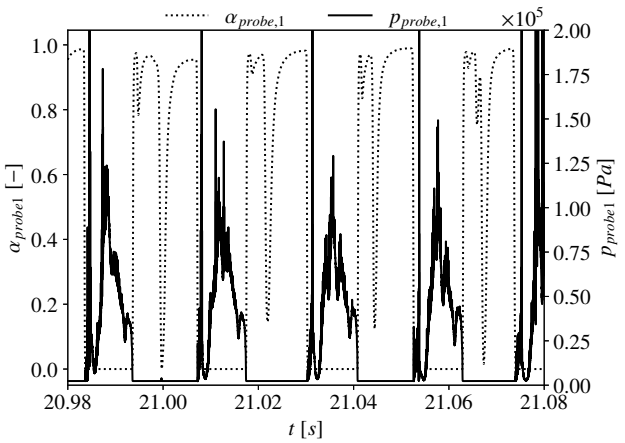

Fig. 11.: Plot of exemplary pressure and void fraction data collected by the probe located 0.01m downstream of the nozzle throat.

The detection of shedding via pressure fluctuations at the domain inlet might however be susceptible to false positives, as the observed variation in pressure could also be caused by oscillations of the attached cavity volume which can occur without the cavity actually detaching. Such behavior has been observed during the implementation and validation phase of the viscosity limiter.

A more direct method to detect shedding events and their frequency is the sampling of void fraction at a probing location downstream of the nozzle throat, as has been done in the experimental work by Reboud et al. using an optical probe.[12] In the presented simulations probing locations are defined 0.01 m, 0.03 m and 0.04 m downstream of the nozzle throat. Figure 10 shows the probe locations alongside the time averaged vapor distribution downstream of the nozzle throat generated from 110 samples taken at 0.01 s intervals.

Close to the throat of the nozzle a persistent region of vapor can be seen. As the goal is the detection of detached vapor pockets traveling downstream, the probing locations are specified further downstream.

Pressure as well as void fraction are sampled and saved at each iteration. A sample of the gathered data is plotted in Fig. 11.

Again, a periodic process can be identified. Figure 12 now compares the void fraction data collected by all three probes for a representative time frame.

While reoccurring detections of vapor are visible for probes one and two, the signal detected by probe three exhibits noticeable variations between the three shown events. Computing the

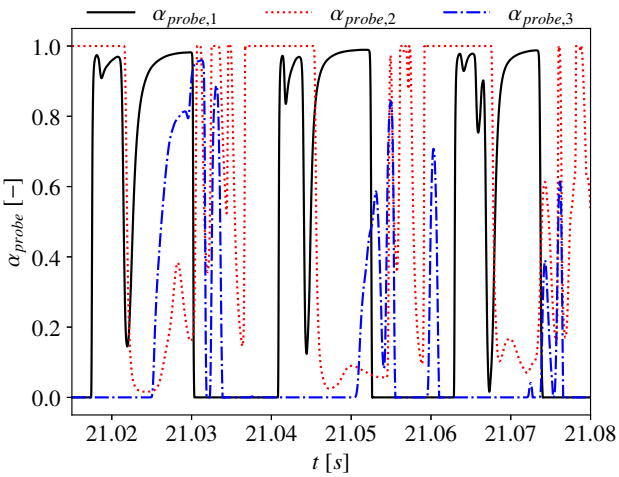

Fig. 12.: Comparison of the void fraction data between the three probed locations.

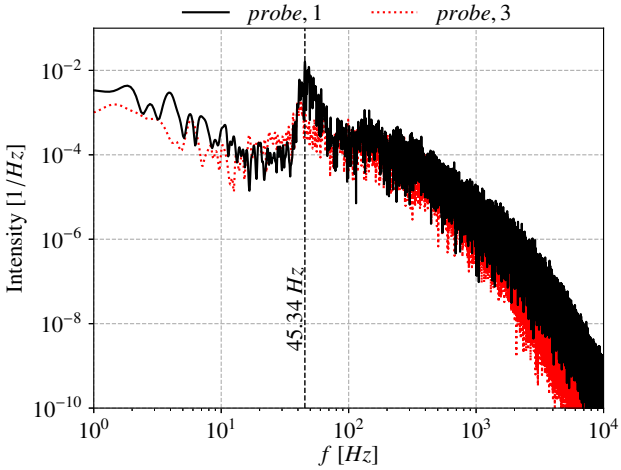

Fig. 13.: PSD-Plot of the void faction data collected by probe 1 and probe 3.

power spectral density for this data again yields a frequency of ca. 45 Hz, as indicated in Fig. 13.

With the evaluation of the time-averaged void fraction data, the resulting selection of probing locations and the detection of a dominant frequency equal to the experimentally reported shedding frequency, it can be concluded, that the modification oft the k-w SST turbulence model enables the reproduction of cloud cavitation.

Finally, the process outlined above is applied to the fine mesh in which no wall functions are applied. The frequency content of the area averaged inlet pressure is presented in Fig. 14.

Analogous to Fig. 13 probe data is processed and presented in Fig. 15.

While a frequency close to 45 Hz can again be clearly identified in the area averaged inlet pressure signal, the probe data is not as conclusive. This may be explained by the considerably lower number of samples that are processed to generate the presented plots, when compared to Fig. 13.

With this, the numerical setup alongside the turbulence and cavitation model configuration described above is accepted as sufficiently capable and stable as to be applied to the full in-

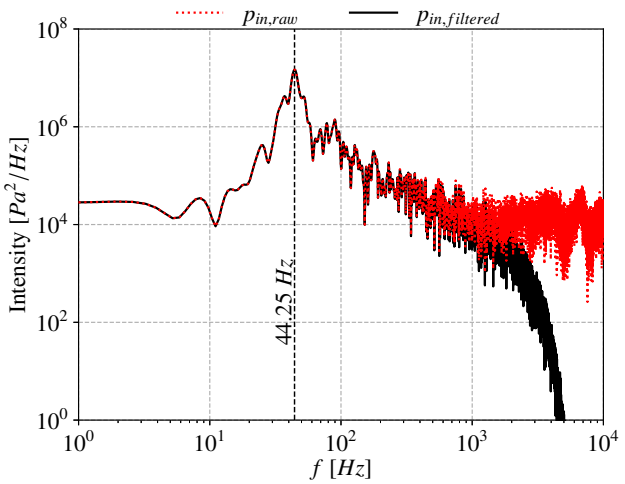

Fig. 14.: PSDPlot of the inlet pressure again indicating a maximum at a frequency of ca. 45 Hz for both filtered and unfiltered pressure data.

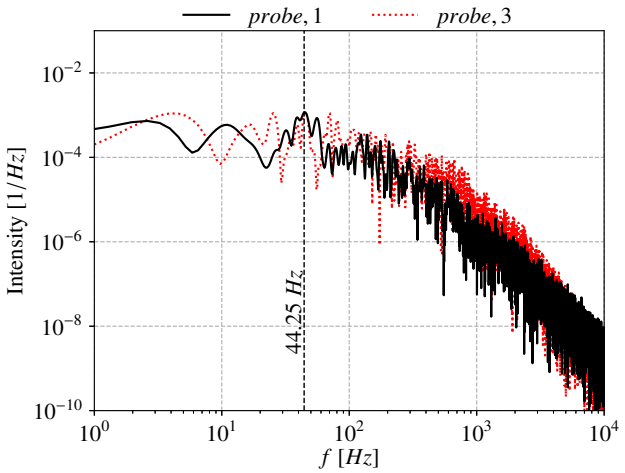

Fig. 15.: PSD-Plot of the void faction data collected by probe 1 and probe 3 during the calculation not utilizing wall functions and employing and overall finer mesh.

ducer geometry. Furthermore, is concluded, that employing wall functions is acceptable when investigating shedding phenomena at inducer blades using the presented approach, allowing for less costly transient simulations.

3. Inducer Flow Simulations

With the successful reproduction of the validation case results the implemented model is now applied to a complete inducer geometry. The geometry examined here, as well as in the preceding paper, is derived from requirements set by the methane pump of the LUMEN rocket engine currently being operated at the German Aerospace Center's Institute of Space Propulsion in Lampoldshausen.[19] The inducer features a constant blade angle, 0° cant angle and no swept leading edges. Furthermore, tip gap leakage is not considered. Design parameters and operating conditions considered in the presented simulations are listed in table 2.

Table 2.: Inducer design parameters.

Parameter	Value
Hub diameter	20 mm
Shroud diameter	31.8 mm
Mass flow at outlet	2.8 kg/s
Rotational rate	43500 RPM
Blade angle at LE Tip	16.3°
Incidence angle	3°
Number of blades	3
Blade thickness	2 mm
Leading edge diameter	0.2 mm
Solidity at blade tip	2.5

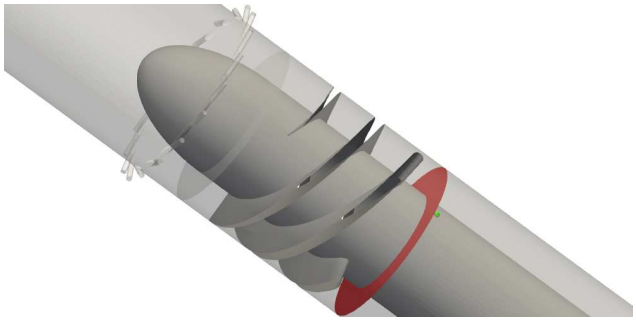

Fig. 16.: Overview of the principal components of the simulation domain. The inducer inlet interface between moving and stationary mesh regions is indicated by an opaque disk while the outlet interface, at which area averaged pressure samples are extracted, is represented by a red disk. The probe location, at which the data discussed below is extracted, is indicated by a sphere just downstream of the inducer outlet interface.

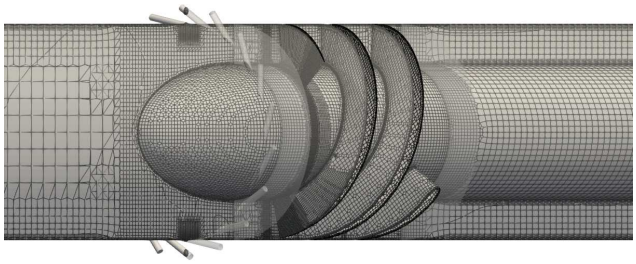

Fig. 17.: View of the inducer and hub surface mesh alongside a cut through the flow domain.

3.1. Simulation Domain and Mesh

Here the simulation domain examined in the preceding paper is reused.[6] It consists of a cylindrical inlet section which features 18 1 mm diameter tangential injectors located 17 mm upstream of the inducer, the inducer and a straight outlet section, as shown in Fig. 16. An overview of the mesh, which is generated using cfMesh included with OpenFOAM, is given in Fig. 17. The location of the holes is chosen according to design constraints imposed by the LUMEN fuel pump. Averaging samples taken over two inducer rotations, the wall dimensionless wall distance plotted in Fig. 18 is obtained.

As the version of of cfMesh used here restricts total inflation layer height to the height of the first adjacent internal cell, a compromise between a desire for a $y_+ \approx 30$ in order to conserve cells resolving gradients in the boundary layer, an expansion ratio of approximately 1.2 and the necessity for refinements in the

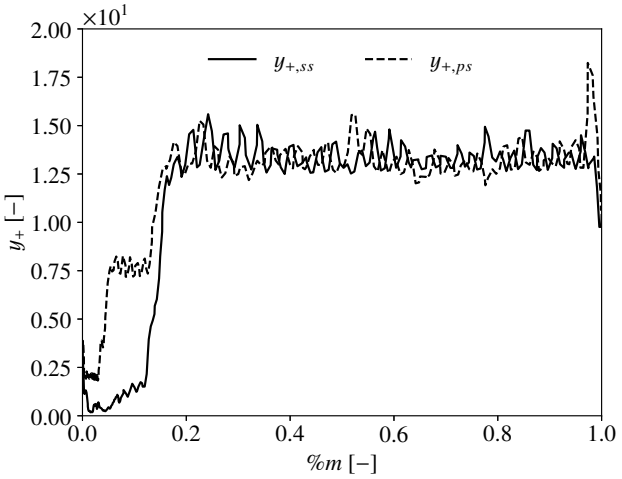

Fig. 18.: Plot of average y_+ at 50% blade height over meridional coordinate for one inducer blade.

region of interest close to the blade leading edge has to be made. This is reflected in the unnecessarily low y_+ values present over the first 20% blade length.

3.2. Numerical Setup

The numerical setup described in section **2.3.** is generated by iterating between the model validation case simulation and the simulation of the full inducer geometry. Here the goal is a setup which allows for both the reproduction of the shedding frequency reported for the validation case geometry as well as a flow field exhibiting minimal spurious oscillations for the complex geometry of the full inducer. As with the calculations presented in the preceding paper, the selection of appropriate inlet and outlet boundary conditions for pressure and velocity require special consideration. It is suggested to impose inlet velocity and outlet pressure in order to suppress oscillations at the outlet boundary. This setup is employed to obtain an initial solution for the inlet flow rotation free case. However, as the introduction of flow rotation in the inlet reduces the inducer's capability to produce head, this configuration is not suitable for a comparison where identical inlet pressures are desired. The imposed outlet pressure would have to be manually be adjusted until identical inlet pressures are present in both cases. It is decided to apply identical fixed static pressures at the domain inlets while enforcing a fixed average outlet velocity via the flowRateOutletVelocity boundary type. This has shown to produce stable results while also allowing for the definition of identical inlet pressures among the evaluated cases. Furthermore, this configuration maintains identical volume flows at the inducer inlet independent of the presence and magnitude of a radially injected volume flow.

Based on the analysis performed in the preceding publication, the velocity at which fluid enters the simulation through the tangential injection holes is set to 50 m/s.

As the influence of wall functions has been found to be negligible in the validation case simulations, they are also applied here. For both the main and tangential inlets turbulence kinetic energy and turbulence specific dissipation rate values are defined. A turbulence intensity of 5% is assumed while turbulence specific dissipation rate is based on a turbulence length scale calculated according to equation 10 where d_h is the hydraulic diameter of the main inlet or the tangential inlets, if applicable.

$$l = 0.038 d_h \tag{10}$$

The connection between static and rotating mesh regions is facilitated via the cyclicAMI boundary condition. While this is a standard boundary type, it is susceptible to mesh misalignment which has to be addressed by increasing circumferential mesh resolution at the interfaces.

A summary of the employed boundary condition types is given in table 3

Table 3.: Inducer simulation boundary conditions with tangential injection of fluid in the inlet. Otherwise the tangential inlet velocity is set to noSlip wall.
CA = cyclicAMI, FFP = fixedFluxpressure, FOV = flowRateOutletVelocity, FV = fixed value, IO = inletOutlet, KQR = kqRWallFunction, MWV = movingWallVelocity, NS = noSlip, OWF = omegaWallFunction, PIA = pressureInletOutletVelocity, SNF = surfaceNormalFixedValue, TIK = turbulentIntensityKineticEnergyInlet, TMF = turbulentMixingLengthFrequencyInlet, ZG = zeroGradient

Surface	p	U	α	k	ω
inlet	FV	PIA	FV	TIK	TMF
stationary walls	FFP	NS	ZG	KQR	OWF
tangential inlets	FFP	SNF	FV	TIK	TMF
rotating walls	FFP	MWV	ZG	KQR	OWF
rotor-stator-interfaces	CA	CA	CA	CA	CA
outlet	FFP	FOV	IO	IO	IO

Due to the more complex geometry and associated flow field, the time step has to be reduced to 2e-7 s in order to not exceed a maximum Courant number of 3.5. While this value is found in the mesh refinement around the tangential injection sites, the mean Courant number lies at approximately 0.05. All other options are identical to the validation case setup described above.

3.3. Discussion of Results

OpenFOAM offers an extensive suit of post processing functions, ranging from the monitoring of e.g. pressures at boundaries or the definition of probe points to user programmed functions which may be executed at user defined intervals. In the following, the amount of vapor throughout the simulation domain is evaluated. This is followed by the analysis of pressure data gathered at a probe located 10 mm downstream of the inducer blade trailing edge in close proximity to the outer outlet wall, approximating a possible pressure sensor position in a physical experiment, as indicated in Fig. 16. Lastly, the area averaged pressure on the inducer outlet interface is evaluated. All measurements are taken at each iteration, resulting in a sample rate of 5 MHz. The flow field in the domain is exported every twenty iterations, or approximately every degree of inducer rotation for two rotations.

3.3.1. Inlet Velocity Distribution

The radial distribution of the circumferential velocity component upstream of the inducer is plotted in Fig. 19. This data is extracted from the 720 domain samples mentioned above. Deviations seen for the samples taken 10 mm and 17 mm upstream of the balde leading edge are caused by the geometry of the inlet channel. Here the channel height increases due to the decreasing shaft diameter. Also, the no-slip boundary condition

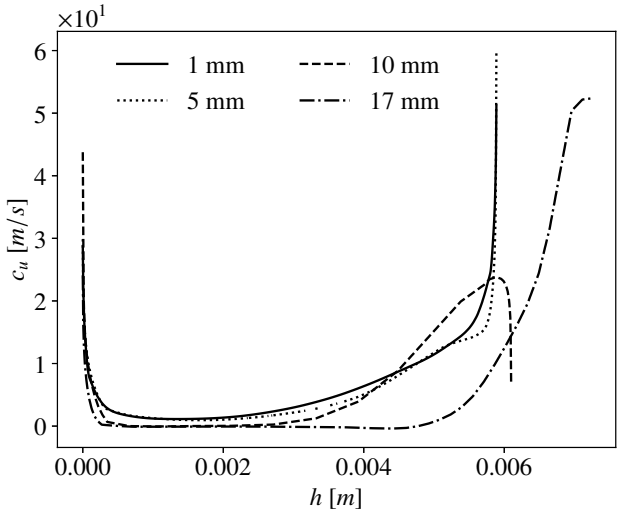

Fig. 19.: Plot of circumferential velocity component c_u over blade height h / inlet channel height for positions 1 mm, 5 mm, 10 mm and 17 mm upstream of the inducer blade leading edges. Here 17 mm aligns with the position of the tangential injection sites.

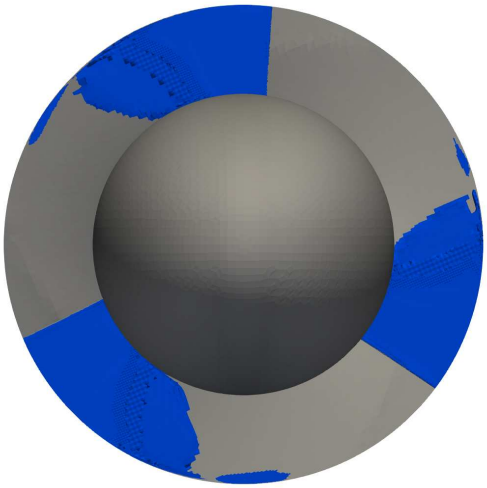

Fig. 20.: View into the inducer inlet for the simulation without inlet swirl. An ISO-Surface, encompassing the volume made up of cells containing at least 0.1% vapor is used to indicate extend of cavitation.

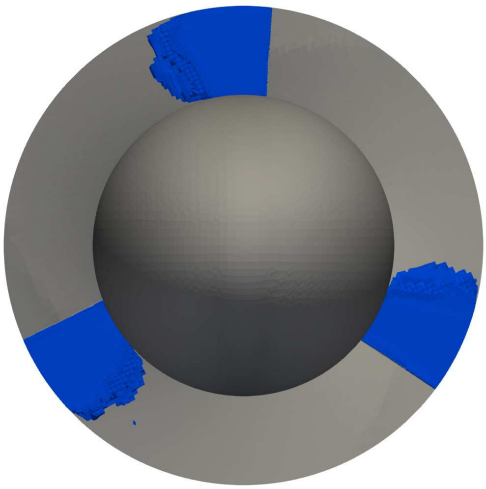

Fig. 21.: Here the vapor distribution along the inducer leading edges is shown for a partially co-rotating inlet flow. This simulation also yielded the results shown in Fig. 19.

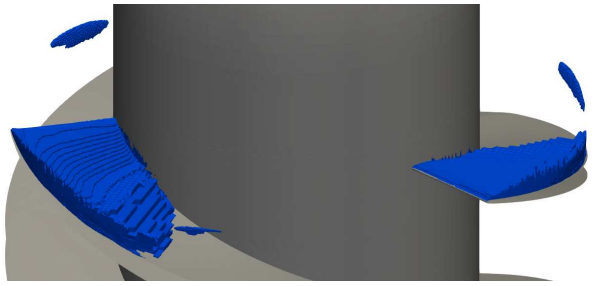

Fig. 22.: View of the void fraction present at the leading edges of the inducer, represented by an ISO-Surface encompassing 0.1% to 100% void fraction for no inlet flow rotation.

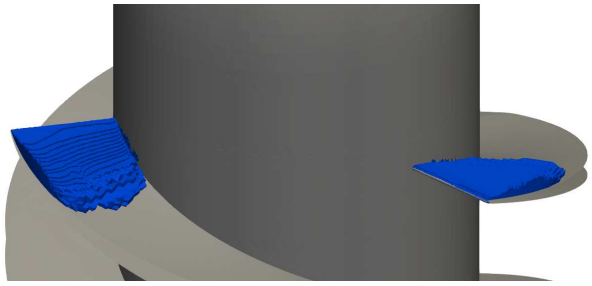

Fig. 23.: View identical to the one presented in Fig. 22 but derived from the simulation including inlet flow rotation.

applied to the outer inlet pipe wall is visible in the velocity decrease seen at the upper end of the data set extracted 10 mm upstream of the blades.

A substantial circumferential velocity component is present over the upper 50% of the blade height as the flow encounters the blade leading edge. Wall velocities of the rotating hub and shroud are also visible for the lower two measurements.

3.3.2. Void Fraction

Averaging the 720 samples taken after the simulation reached a quasi-steady state, the void fraction distribution presented in Figs. 20 to 23 is obtained.

Comparing Figs. 20 and 21 it becomes apparent that the extent of the volume occupied by vapor is altered between the two cases. In Fig. 21 the volume occupied by vapor at the leading edge of each blade exhibits a local minimum at approximately 50% blade height. While the circumferential velocity distribution does diminish to zero at this position, the present vapor volume fraction is substantially reduced.

Evaluating Fig. 20 further, a vapor structure close to the shroud behind each leading edge can be identified. This feature is not present in the inducer exposed to a partially co-rotating inlet flow. This feature is more easily recognized when comparing Figs. 22 and 23 which display the averaged data shown Figs. 20 and 21 at a different angle.

Evaluating the 720 collected flow field samples individually instead of in an averaged form, it can be seen that a shedding process at the blade tips causes the detached vapor presence seen in the averaged results.

Figure 24 shows the development of the domain void fraction over period of 0.005s which is roughly equal to 4 rotations.

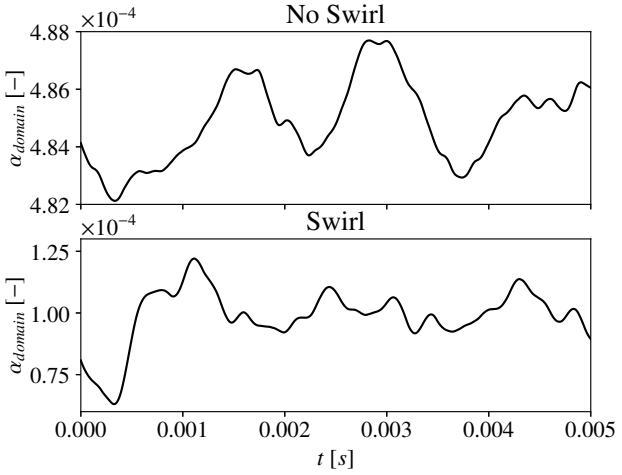

Fig. 24.: Plot of the void fraction present in the entire domain over a duration equal to approximately four rotations for both simulated cases.

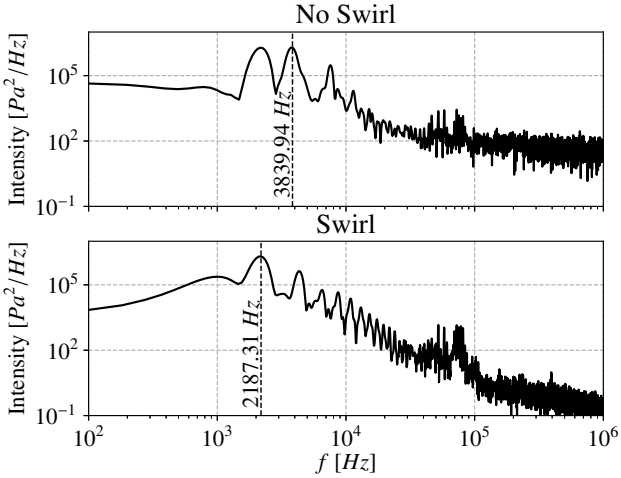

Fig. 26.: Plot of the power spectral density found in the probe data for both simulated cases.

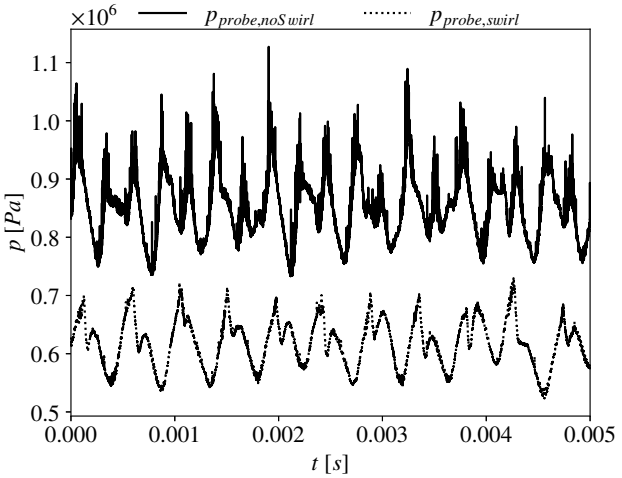

Fig. 25.: Plot of pressure data collected by a probe located 10 mm downstream of the inducer blade trailing edges.

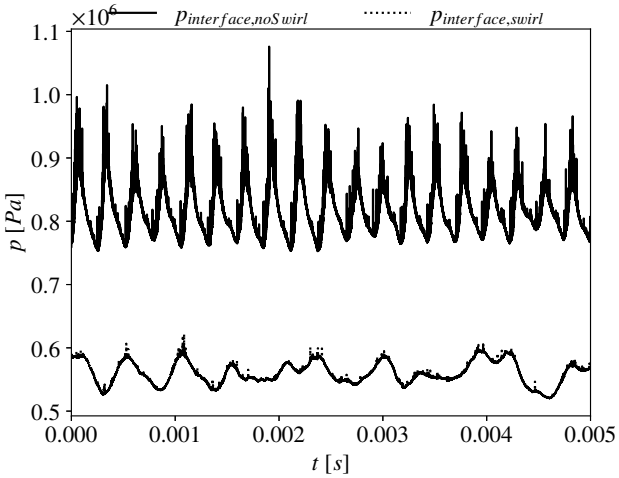

Fig. 27.: Plot the area averaged pressure present at the inducer outlet interface.

It can be seen that the amount of vapor present in the domain is reduced when the flow entering the inducer is forced to rotate in the blade tip region. However, the variation of the void fraction is substantially increased. Again, the evaluation of the non-averaged flow field snapshots makes it apparent that the shorter and therefore thinner vapor sheet is more prone to oscillations while the non-rotating inlet flow causes a cavity of more constant length to form.

The influence of this combination of vapor volume reduction but amplitude fluctuations increase is evaluated by examining pressure data. Figure 25 plots the data collected by the pressure probe described above for the same period of 0.005 s evaluated in Fig. 24.

While the amplitude fluctuations of the domain void fraction would suggest the presence of larger pressure variations, this is found not to be the case. Considering that the blade loading is reduced by the rotating inlet flow, the head rise generated by this inducer is also reduced. Hence a direct comparison of amplitudes might not be applicable. Instead, the frequency content of the recorded pressure data is examined, as done for the validation of the reference case. The results are presented in Fig. 26.

The peak present in both plots at approximately 2180 Hz represents the blade passing frequency at 2175 Hz. Significant differences are found at approximately 3.8 kHz. While the peak dominating the frequency spectrum is found here for the baseline case, it is completely absent when co-rotation in the inlet flow is introduced. Examining the frequency range beyond 10 kHz a reduction in broadband noise is noticeable while the structure of the signal in this region and beyond remain comparable between the two cases.

In order to remove the presence of the blade passing frequency and its harmonics, the area averaged pressure present at the inducer outlet interface is examined in Figs. 27 and 28.

The raw data extracted from the baseline simulation presents a repeating structure while the introduction of inlet flow rotation leads to a more chaotic progression of the outlet pressure over time. Again, the frequency content of both signals is evaluated and again the baseline case exhibits a prominent signal at approximately 3.8 kHz which is completely absent when inlet flow rotation is introduced.

Revisiting the vapor distribution presented in Fig. 20 and 22,

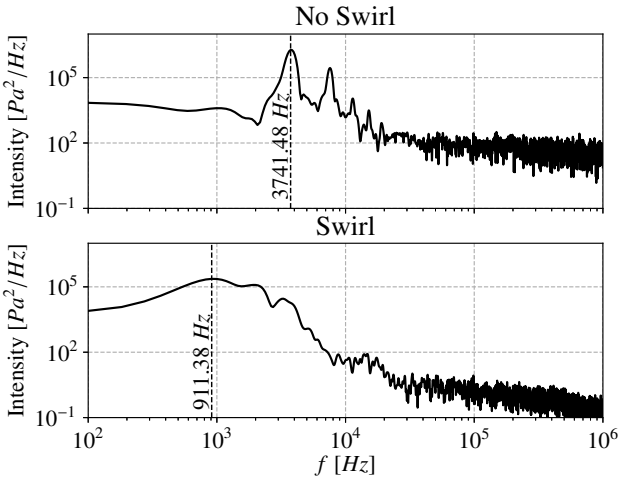

Fig. 28.: Plot power spectral density derived from the data shown in Fig. 27.

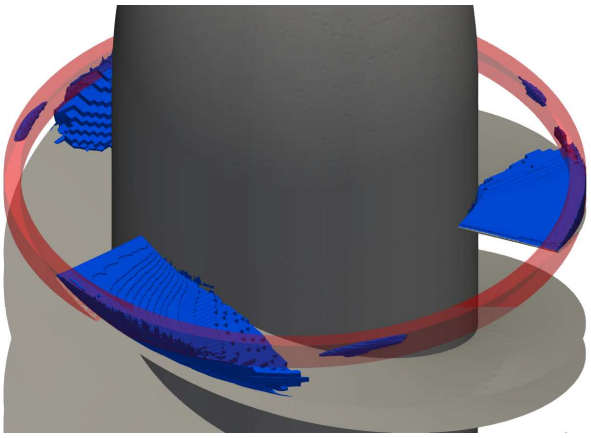

Fig. 29.: View of the averaged vapor distribution at the blade tips for the inlet flow rotation free case. Here the aforementioned control volume around the region of interest is indicated by a translucent red ring.

it is suspected that the shedding process at the blade tips might be the source for the 3.8 kHz signal present in both the pressure probe and area averaged interface pressure data. In order to evaluate the impact of any process taking place in this area a control volume is defined, as shown in Fig. 29.

The void fraction present in this control volume is extracted for each of the 720 samples taken of the complete flow domain. The gathered data is presented in Fig. 30.

While only 720 data points are gathered in this way, a PSD plot indicates, that the observed 3.8 kHz pressure signal is reflected in the variation of the amount of vapor sampled in the cylindrical control volume, as shown in Fig. 31.

4. Conclusion and Outlook

Based on preceding steady state simulations, an advantage of partial inlet flow rotation concerning inducer stall could not be found when compared to an identical machine operating on a purely axial inlet velocity profile. It was therefore decided to investigate the impact of partial inlet flow rotation utilizing transient simulations. OpenFOAM was selected both due to its availability on DLRs HPC infrastructure and versatility. Modi-

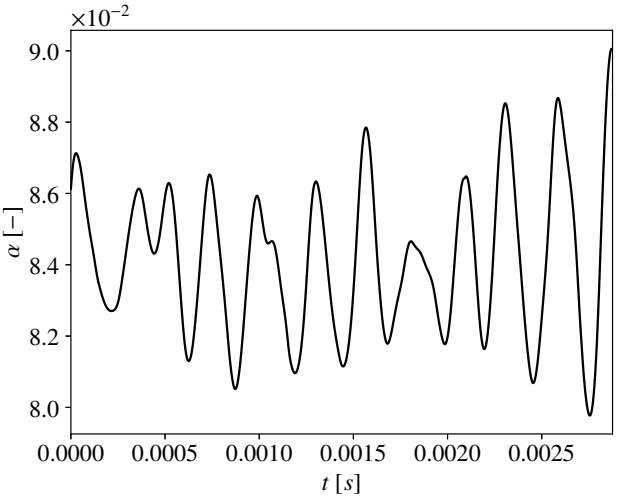

Fig. 30.: Plot of vapor volume fraction over the duration of the 720 full flow domain samples.

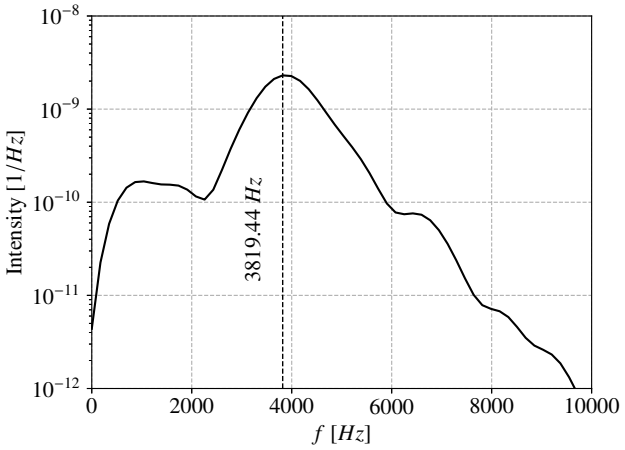

Fig. 31.: PSD-Plot of the data presented in Fig. 30.

fications to the k-w SST turbulence model included in OpenFOAM were implemented in order to enable the simulation re-entrant jet driven cavity shedding. Experimentally observed shedding frequencies reported in literature for a simplified inducer blade geometry in water could be reproduced. A numerical setup combining accuracy as well as tolerance for mesh imperfections, unavoidable in complex pump geometries, could be identified. The setup is the applied to a previously evaluated inducer geometry, representative of DLR's LUMEN liquid natural gas fuel turbopump. Evaluating averaged flow field data as well as pressure data sampled every iteration it is found that:

- The vapor volume fraction decreases with partially co-rotating inlet flow
- The amplitude fluctuation of the vapor volume present at the inducer blades increases
- For the evaluated inlet pressure of 5 bar a shedding process present at the inducer blade tips in the inlet flow rotation free case could be suppressed
- A dominant peak in power spectral density of the inducer outlet pressure could be suppressed by modifying the shedding behavior of the attached cavity in the blade tip region
- Broadband noise in the inducer outlet pressure at approximately 30 kHz is reduced with the introduction of partial

inlet flow co-rotation

Furthermore, the potential of OpenFOAM as a tool for pump simulation and test preparation has been shown.

Building on these results and considering that the presented results represent a work in progress, activities are ongoing to address several shortcomings. Firstly, the origin of the 3.8 kHz signal present in the baseline simulation is to be further investigated. To this end meridional cuts at 95%, the position of the observed shedding events, as well as ca. 50% blade height, the position of the minimal extent of the attached cavity, are to be extracted and evaluated using dynamic mode decomposition, a technique commonly applied in the analysis of combustion instabilities at DLR's Lampoldshausen site. With this the flow phenomena associated with the identified frequency can be identified, allowing for a more detailed insight into whether the observed cloud cavitation is cause for or effect of the observed 3.8 kHz signal.

An inducer design exhibiting swept leading edges and a varying blade angle, aimed a pressure rise of 7 bar, has been designed for the LUMEN fuel turbopump and is currently being manufactured. With the recent commissioning of the turbopump technology group's modular turbopump test bench, this inducer is to be examined experimentally. The obtained data is intended to be utilized as reference for a future simulation campaign. Before these test take place, the simulation work flow described in this publication is also to be applied to this inducer. The generated data may aid in the definition of operating points for the experimental campaign. It may also serve as a starting point for the investigation of the impact of partially rotating inlet flow on this inducer's ability to generate head. The impact reported here for an inducer with constant blade angle makes partial inlet flow co-rotation as a means of cavitation control not piratical.

In anticipation of the planned test activities, the presented numerical method is to be applied to this inducer geometry to both identify operation conditions of interest as well as further examine possible sources for the 3.8 kHz signal identified in this study. Here the flow around the blunt trailing edges is to be examined, as vortex shedding could be a source of parts of the noise observed in the pressure data.

Lastly, computational resources available at DLR via the CARO-cluster now also enable the extension of a preceding study of the inlet section of the inducer based on detached eddy simulations to the entire machine, making additional empirical corrections in the utilized turbulence models unnecessary.

Acknowledgments

The authors gratefully acknowledge the scientific support and HPC resources provided by the German Aerospace Center (DLR). The HPC system CARO is partially funded by "Ministry of Science and Culture of Lower Saxony" and "Federal Ministry for Economic Affairs and Climate Action".

References

1) Japikse, D.: Overview of Industrial and Rocket Turbopump Inducer Design, 11th International Symposium on Cavitation, Daejeon, South Korea, CAV2001:sessionB7.001, 2001.
2) Sutton, G. P. and Biblarz, O.: *Rocket propulsion elements*, John Wiley & Sons, New York, 2016.
3) Brennen, C. E.: *Hydrodynamics of Pumps*, Cambridge University Press, New York, USA, 2011.
4) Acosta, A. J., Tsujimoto, Y., Yoshida, Y., Azuma, S., and Cooper, P.: Effects of leading edge sweep on the cavitating characteristics of inducer pumps, *J. Rot. Mach.*., **7(6)** (2001), pp. 297–301.
5) Sun, Q., Ji, C. and Fang, J.: Optimization Design of IGV Profile in Centrifugal Compressor, *Mathematical Problems in Engineering*., **2017** (2017), pp. 1–9.
6) Groll, C., Traudt, T., Oschwald, M., Schlechtriem, S., Herbertz, A.: Inducer Cavitation Control via Inlet Swirl, 33rd International Symposium on Space Technology and Science, Beppu, Japan, 2022.
7) Coutier-Delghosa, O., Fortes Patella, R., Reboud, J., Stutz, B.: Test case n°30: Unsteady cavitation in a Venturi type section (PN), *Multiphase Science and Technology*., **16** (2005), pp. 207–218.
8) d'Agostino, L.: *Cavitation Instabilities and Rotordynamic Effects in Turbopumps and Hydroturbines*, Springer, Cham, Switzerland, 2017, pp. 200–202.
9) Stutz, B. and Reboud, J. L.: Experiments on unsteady cavitation, *J. Experiments on unsteady cavitation. Experiments in Fluids*., **22** (1997), pp. 191–198.
10) Zwart, P., J.,Gerber, A., G., Belamri, T.: A Two-Phase Flow Model for Predicting Cavitation Dynamics, Proceedings of International Conference on Multiphase Flow, Yokohama, Japan, 2004.
11) Decaix, J., Goncalvès, E.: Compressible effects modelling in turbulent cavitating flows, *European Journal of Mechanics*., **39** (2013), pp. 11–31.
12) Reboud, J. L., Stutz, B. and Coutier, O.: Two-Phase Flow Structure of Cavitation: Experiment and Modelling of Unsteady Effects, 3rd International Symposium on Cavitation, Grenoble, France, 1998.
13) Reboud, J. L., Coutier, O., Pouffary, B., Fortes-Patella, R.: Numerical Simulation of Unsteady Cavitating Flows: Some Applications and Open Problems, 5th International Symposium on Cavitation, Osaka, Japan, 2003.
14) Menter, F. R., Kuntz, M., and Langtry, R.: Ten years of industrial experience with the SST turbulence model, Proceedings of the fourth international symposium on turbulence, heat and mass transfer, Antalya, Turkey, 2003, pp. 625–632.
15) Groll, C., Traudt, T., Oschwald, M., Schlechtriem, S.: Cavitation Prediction in the LUMEN LCH4 Pump, 11th International Symposium on Cavitation, Daejeon, South Korea, 2001.
16) Schnerr, G. H., and Sauer, J.: Physical and Numerical Modeling of Unsteady Cavitation Dynamics, Proceedings of the 4th International Conference on Multiphase Flow, New Orleans, USA, 2001.
17) Warming, R. F., and Beam, M.: Upwind Second-Order Difference Schemes and Applications in Aerodynamic Flows, *AIAA J.*, **14** (1976), pp. 1241–1249.
18) Virtanen, P., Gommers, R., Oliphant, T. E.: SciPy 1.0: Fundamental Algorithms for Scientific Computing in Python, *Nature Methods*., **17(3)** (2020), pp. 261–272.
19) Traudt, T., Armbruster, W., Groll, C., dos Santos Hahn, R., Dresia, K., Börner, M., Klein, S., Suslov, D., Müller, M., Kurudzija, E., Haemisch, J., Deeken, J., Hardi, J., Schlechtriem, S.: LUMEN: Liquid Upper Stage Demonstrator Engine - A Versatile Test Bed for Rocket Engine Components: Hot-Fire Test Results, 75th International Astronautical Congress (IAC), Milan, Italy, IAC-24-AC4.1.5.x86850, 2024.